Paper Number: **1706**

Title: **A Modified Edge Crack Torsion Test for Measurement of Mode III Fracture Toughness of Laminated Tape Composites**

Authors: Michael W. Czabaj
Barry D. Davidson
James G. Ratcliffe

**ABSTRACT**

Modifications to the edge crack torsion (ECT) test are studied to improve the reliability of this test for measuring the mode-III fracture toughness, $G_{IIIc}$, of laminated tape fiber-reinforced polymeric (FRP) composites. First, the data reduction methods currently used in the ECT test are evaluated and deficiencies in their accuracy are discussed. An alternative data reduction technique, which uses a polynomial form to represent ECT specimen compliance solution, is evaluated and compared to FEA results. Second, seven batches of ECT specimens are tested, each batch containing specimens with a preimplanted midplane edge delamination and midplane plies with orientations of $+\theta/-\theta$, with $\theta$ ranging from 0° to 90° in 15° increments. Tests on these specimens show that intralaminar cracking occurs in specimens from all batches except for which $\theta$ = 15° and 30°. Tests on specimens of these two batches are shown to result in mode-III delamination growth at the intended ply interface. The findings from this study are encouraging steps towards the use of the ECT test as a standardized method for measuring $G_{IIIc}$, although further modification to the data reduction method is required to make it suitable for use as part of a standardized test method.

---

Michael Czabaj, Department of Mechanical Engineering, University of Utah, Salt Lake City, Utah 84112, USA.
Barry D. Davidson, Professor, Department of Mechanical and Aerospace Engineering, Syracuse University, Syracuse, New York 13244, USA.
James Ratcliffe, NASA Langley Research Center, Hampton, VA, 23681, USA.

## INTRODUCTION

The relatively low toughness and strength of matrix materials used in laminated fiber-reinforced polymeric (FRP) composites makes these material systems susceptible to damage from transverse loading [1]. A common damage type arising from such a scenario is delamination. Although mode-I loading conditions tend to be most critical from a crack growth viewpoint, delamination growth in FRP composites may also occur under mode-II (in-plane shear) and mode-III (anti-plane shear) loading, or some combination of the three. Procedures for characterizing the onset of delamination growth are commonly based on the critical strain-energy release rate, $G_c$, which is associated with a particular delamination mode or mode-mixity. Methods for measuring $G_c$ associated with mode-I, mode-II, and mixed mode-I/II delamination at unidirectional ply interfaces are well established and are available as standardized tests [2-4]. Although many test methods have been proposed for measuring the value of $G_c$ associated with mode-III loading, identifying the candidate test most suitable for standardization has proven difficult. A number of studies have considered various split beam geometries [5-7], but the majority of work in this area has focused on the edge crack torsion (ECT) test [8].

The ECT test geometry is depicted in Fig. 1. The specimen is rectangular and fabricated from composite tape material. It contains a preimplanted polytetrafluoroethylene (PTFE) insert located at the specimen midplane and spanning the specimen's length along one edge, as shown in Fig. 1. The specimen is twisted via equal-and-opposite couples, resulting in mode-III dominated crack-tip stresses acting along the insert's front. The two plies bounding the insert are typically oriented such that their fiber direction is parallel to the expected direction of delamination advance (90º orientation in Fig. 1) [8]. This is consistent with the mode-I, mode-II and mixed-mode-I/II delamination toughness tests [2-4], for which delamination growth is in the direction of the adjacent plies.

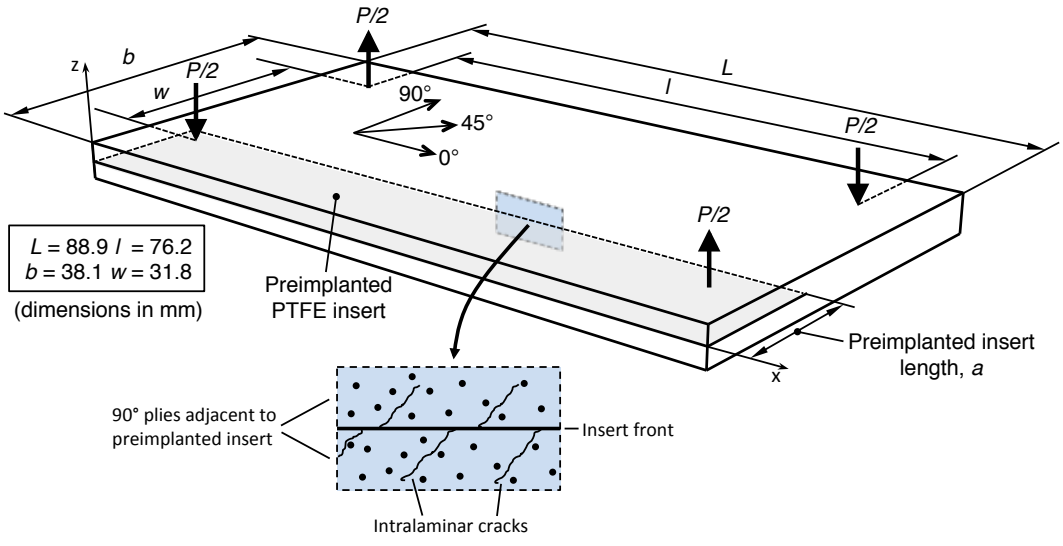


Figure 1. The ECT test specimen geometry

The ECT test procedure involves loading the specimen until delamination advance is detected. However, delamination growth in these specimens occurs internally and visual observations cannot be used to determine growth initiation. Delamination advance is instead inferred from the specimen loading response, in which delamination advance is indicated by a gradual or sudden load drop. Several specimens are tested, each with a preimplanted insert of different length, $a$, which is defined in Fig. 1. The relationship between initial specimen compliance and insert length is established from these test results using a procedure referred to as multi-specimen compliance calibration (MSCC). The compliance relationship and load drop at delamination onset are used with linear elastic fracture mechanics (LEFM) to determine the mode-III fracture toughness, $G_{IIIc}$, of each specimen.

If the identified load measurements accurately correspond to the initiation of delamination advance from the preimplanted insert, for a given material system, each specimen should exhibit the same value of $G_{IIIc}$; i.e., no R-curve or other effects should be present to cause $G_{IIIc}$ to differ between specimens. However, studies of the ECT test indicated that $G_{IIIc}$ measurements did indeed differ between specimens [8, 9]. Moreover, in [10], $G_{IIIc}$ was found to exhibit significant dependency on insert length, and was higher in specimens with longer inserts. This was attributed to varying amounts of damage formation (in particular ply splitting) prior to the assumed moment of delamination initiation. This damage formation was inferred from observed nonlinearity of specimen loading response prior to delamination initiation. In later work, other researchers also reported nonlinear ECT loading response and dependency of $G_{IIIc}$ on insert length [11-15], with various explanations suggested, including ply splitting and R-curve effects.

A recent re-examination of the ECT test focused on determining the precise cause of these $G_{IIIc}$ variations [16]. Here, ECT specimens were loaded until a nonlinear loading response was observed, but before delamination advance was detected. Specimens were then examined using ultrasonic transmission and X-ray computed tomography methods, in addition to being destructively sectioned for examination using optical microscopy. These examinations revealed a series of intralaminar matrix cracks that initiated from the insert front region, growing at approximately 45° to the specimen plane through the 90° plies adjacent to the preimplanted insert, as illustrated in Fig. 1. The cause of these cracks is thought to be the resolved tensile component of the stress state that arises in the ECT specimens along the delamination front. Because the fibers of the 90° plies adjacent to the insert do not cross the path of these cracks, the cracks grow unimpeded through these plies until they reach a ply whose fibers can arrest their growth. This process, which occurred in the ECT specimens studied in [16], resulted in delaminations migrating to ply interfaces other than the intended delamination growth interface of the specimens (the midplane). This migration mechanism has been observed previously in other tape laminates through fractographic analysis [17], which supports findings of the ECT re-examination [16]. Furthermore, a very similar type of unimpeded intralaminar cracking was observed in split cantilever beam specimens, which were also intended for measuring $G_{IIIc}$ of FRP composites [18].

These recent findings show that attempts at measuring $G_{IIIc}$ using the ECT specimen (and other specimen types) were unsuccessful because the plies neighboring the preimplanted insert were not able to contain the intralaminar

cracking arising from the insert-front stress state. However, containment of these cracks may be possible if the orientation of the plies neighboring the preimplanted insert in an ECT specimen is altered in a manner that promotes the intended mode-III driven delamination growth. The objective of the current study was to explore this possibility and determine what range of ply orientations, if any, could contain intralaminar cracking and thus encourage mode-III delamination growth. To this end, seven groups of ECT specimens were tested. In each group of specimens, the two plies adjacent to the preimplanted insert had orientations of $+\theta/-\theta$, with $\theta$ ranging from 0° to 90° degrees, in 15° increments.

The ECT specimen fabrication, testing, and data reduction procedures are described in the following section. Methods used to evaluate $G_{IIIc}$ associated with delamination initiation and propagation are described. The use of non-destructive ultrasonic inspection for determining the damage state in each group of specimens is detailed. The paper concludes with a discussion of the results and a proposed ECT specimen configuration and data reduction method for measurement of $G_{IIIc}$.

## SPECIMENS AND FABRICATION

The ECT specimens were cut from seven 305x305 mm square plates of 130 gsm IM7/8552 carbon/epoxy pre-preg. During fabrication, each plate was debulked at room temperature and subsequently cured in a hot press, per the recommended cure cycle from the pre-preg manufacturer [19]. The plates were 32-plies thick and the average thickness of all plates was 3.80 mm with standard deviation of 0.01 mm. The stacking sequence of the seven plates was $[-\boldsymbol{\theta}/\{45/(-45)_2/90/(45)_2/-45\}_S/\boldsymbol{\theta}\,\|\,-\boldsymbol{\theta}/\{45/(-45)_2/90/(45)_2/-45\}_S/\boldsymbol{\theta}]$, where $\theta$ varied for each plate, ranging from 0° to 90°, in 15° increments. In the stacking sequence above, the "||" symbol designates the location of the 13μm thick PTFE insert. With respect to the effect of fiber orientation on intralaminar crack containment, $+\theta/-\theta$ and $\theta/\theta$ interfaces are expected to be equivalent. However, the $+\theta/-\theta$ orientation may lessen the effect of fiber nesting on crack face sliding during mode-III loading; thus only this orientation was considered in this study. Due to the slight asymmetry in plates with $\theta \neq 0°$ or 90°, the stretching-twisting coupling terms ($B_{16}$ and $B_{26}$) are nonzero; however, these terms are quite small and their influence on the laminate's behavior is expected to be negligible. Also, the tested laminate is specially orthotropic, thus the bend-twist couplings, ($D_{16}$ and $D_{26}$) are zero, which is important for encouraging a pure mode-III driving force along the delamination front. No warpage of either plate was observed on cool-down or during cutting.

Each plate was cut into ECT specimens as indicated by the red dashed lines in Fig. 2. The heavy square in the figure represents the plate's outer boundary, and the shaded regions represent the PTFE inserts. As indicated in the figure, each plate produced three groups of seven specimens, with normalized insert lengths, $a/b$, ranging from 0.10 to 0.50, in increments of approximately 0.07. Nominal specimen dimensions are as shown in Fig. 1. Note that, after specimen machining, the actual insert lengths (i.e., initial crack lengths) varied slightly from the intended dimensions.

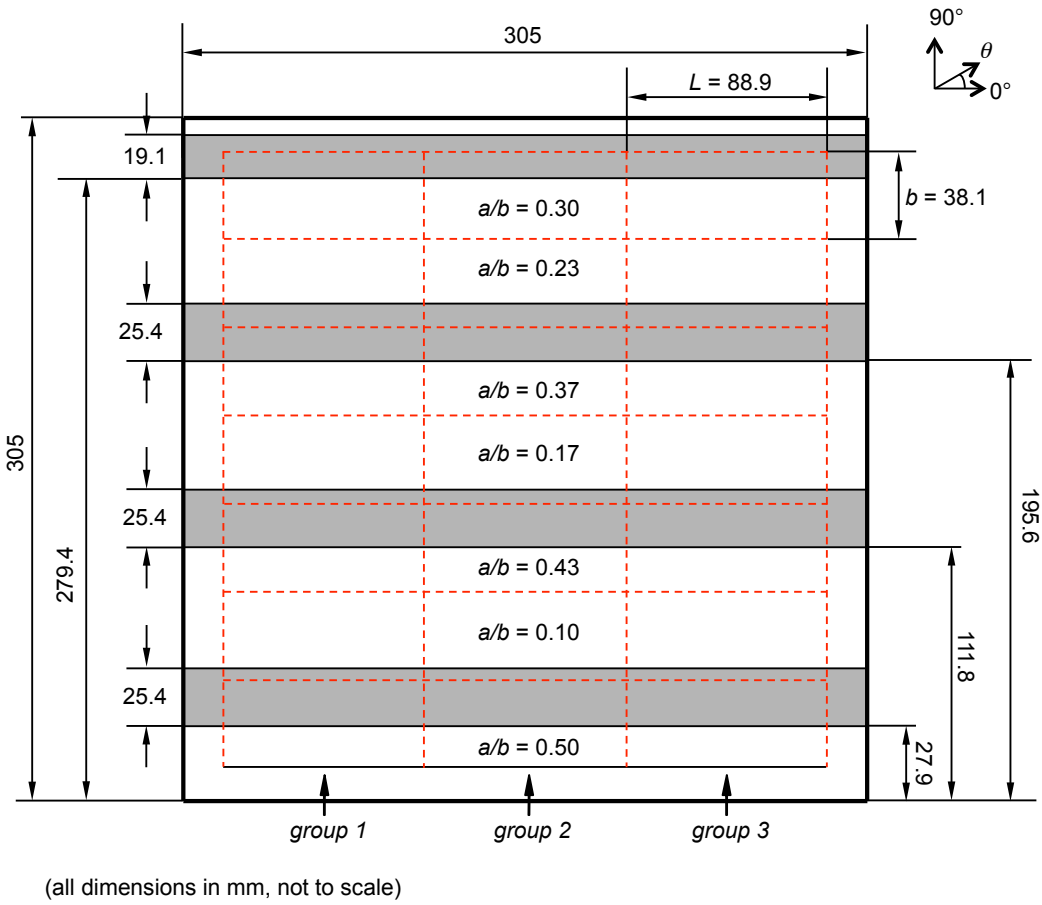


Figure 2. ECT specimen plate layout. Shaded regions correspond to the preimplanted PTFE inserts at the midplane.

## FINITE ELEMENT ANALYSIS

The finite element (FE) analysis presented herein was used to assess the accuracy of the existing data reduction methods used for the ECT test [8, 10], and to propose an alternative method. To this end, seven ECT geometries were modeled, each with a normalized insert length, $a/b$, ranging between 0.1 and 0.5, in increments of approximately 0.07. For reasons which will be discussed later, FE analysis was performed only on specimens with $\theta = 30°$. The FE analysis of the ECT specimen geometry followed the approach outlined in [10]. The FE simulations were performed using the commercial FE code Abaqus® 6.12. Calculation of the strain energy release rate (SERR) components along the delamination front was based on the virtual crack closure technique (VCCT) [20, 21].

The ECT specimen geometry was discretized using 8-noded brick elements (Abaqus® designation C3D8i). An example of the finite element model used to analyze the ECT specimen is presented in Fig. 3. The orthotropic ply properties of IM7/8552 were taken from [10]. Following the approach presented in [10, 21], two plies on each side of the midplane were discretized using one element per ply. The

edge delamination was created by generating two groups of coincident nodes, each connected to elements above and below the delamination plane. A rigid

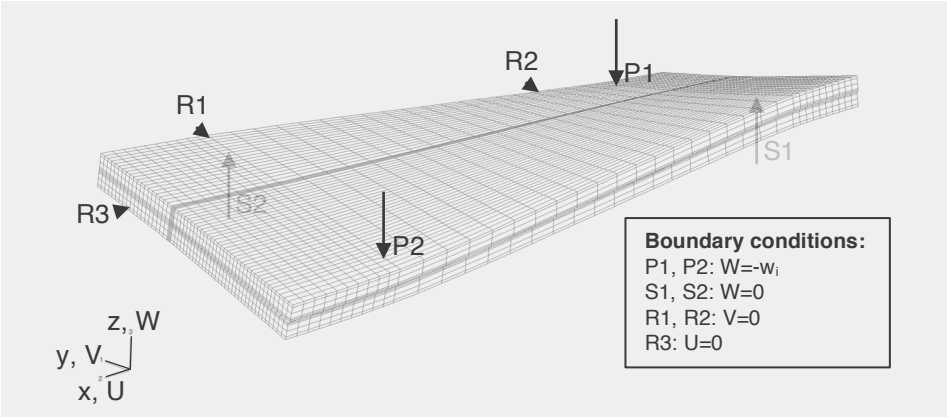


Figure 3. Finite element model of ECT specimen.

contact algorithm was used in the delaminated region to prevent interpenetration of elements along the normal direction. Relative sliding between points in the delamination region was assumed frictionless. Displacement, $w_i$, in the z-direction was applied at the two nodes corresponding to the point of contact of the loading pins (P1 and P2 in Fig. 3) until the resulting total strain energy release rate, $G_T$, calculated using VCCT, equaled 0.1 kJ/m$^2$. Two nodes positioned at the locations of the support pins (S1 and S2 in Fig. 3) were constrained from displacement in the z-direction, to represent contact between the specimen and the pins. Three additional nodes on the periphery of the specimen (R1 – R3 in Fig. 3) were restrained in the x or y directions to prevent rigid body motion. Resulting reaction forces at these nodes were negligible. All boundary conditions used in the analyses are illustrated in Fig. 3.

The FE analyses were used to calculate specimen compliance, $C$, by dividing the applied displacement by the sum of the z-direction reaction loads at locations S1 and S2 (the support pins). These data were used in the multi-specimen compliance calibration (MSCC) approach described in the Introduction section, to calculate a globally derived value of $G_T$ for each specimen (i.e., each $a/b$ value) analyzed. The following four expressions were used to compute $G_T$ as part of the MSCC approach:

$$G_T = \frac{mCP^2}{2lb\left[1 - m(a/b)\right]} \tag{1}$$

$$G_T = \frac{mCP^2}{2Lb\left[1 - m(a/b)\right]} \tag{2}$$

$$G_T = \frac{P^2}{2L}(2p_{ii}a + p_i) \tag{3}$$

$$G_T = \frac{P^2}{2L}(3p_3a^2 + 2p_2a + p_1) \quad (4)$$

Equation 1 is the expression for $G_T$ introduced in [8], where the parameter $C$ is ECT specimen compliance and $m$ is a constant derived from a linear fit between $C$ and $a/b$. Equation 2 is a corrected version of Eq. 1 in which specimen width, L, is used instead of loading pin distance, $l$. The purpose of this correction is to allow for the contribution of the entire specimen width to the specimen compliance. Equation 3 is an expression for $G_T$ based on a 2nd-order relationship between specimen compliance and $a/b$. Equation 4 is an expression for $G_T$ based on a 3rd-order relationship between specimen compliance and $a/b$. The coefficients, $p_n$, in Eqs. 3 and 4, are those of the respective polynomial fits used for the relationship between specimen compliance and $a/b$.

$G_T$ was also calculated using VCCT, where $G_T = G_I + G_{II} + G_{III}$. (Note, the ECT specimen exhibits small amounts of mode-I and mode-II contributions to crack driving force.) $G_T$ calculated from VCCT was used as a baseline to assess the MSCC approaches.

## EXPERIMENTAL PROCEDURE

As shown in Fig. 2, a single ECT plate yielded three groups of seven specimens, with each group containing specimens with normalized insert lengths, $a/b$, from 0.1 to 0.5. The test matrix for each plate is given in Table I. Specific details of the ECT test fixture are given in [16].

Table I. SUMMARY OF TEST MATRIX

| **Midplane interface angle, $\theta$** | **Number of specimens tested** |
|---|---|
| 0° | **7** |
| 15° | **21** |
| 30° | **21** |
| 45° | **7** |
| 60° | **7** |
| 75° | **7** |
| 90° | **14** |

Specimens were tested quasi-statically, in displacement control, at a loading rate of 0.25 mm/min. The specimen loading response was monitored and when a drop in force was observed, indicating delamination growth, the specimen was unloaded. The applied force and fixture displacement were recorded at one-second intervals throughout each test. Initially, one group of seven specimens from each plate (group 2 in Fig. 2) was tested, and subsequently inspected with an ultrasonic C-scan unit equipped with a 10 MHz pulse-echo transducer. After nondestructive inspection, all remaining specimens from the +15°/-15° and +30°/-30° plates, and one group of seven specimens from the 90°/90° plate, were tested as shown in Table I. After

completion of all tests, a few selected specimens from each of the seven plates were sectioned and examined under an optical microscope, as described in [16].

## RESULTS AND DISCUSSION

### FE-based evaluation of data reduction methods

Because the stacking sequence of the ECT specimens is asymmetric, a preliminary set of FE analyses was performed to examine the effect of cure-induced thermal residual stresses on the magnitude of SERR along the delamination front. For all ECT geometries (i.e., all "$\theta$'s), the cooldown from 180°C to 20°C resulted in negligible increase in $G_T$, and thus thermal residual stresses were not considered in subsequent simulations. The following discussion is based on FE analysis of ECT specimens with $\theta = 30°$. The overall conclusions reached for this geometry are expected to be quantitatively similar for geometries with other $\theta$s, thus those are not included here for brevity.

Figure 4 depicts the distribution of mode-III SERR in the ECT specimen (calculated using VCCT) as a function of normalized position across the initial delamination front, *x/L*. In this figure, each distinct symbol corresponds to a different normalized insert length, *a/b*. Vertical dashed lines indicate the location of the support and loading pins. As discussed previously [9, 10, 15], for large values of *a/b*, the distribution of SERR in-between-the-pins (IBP) is either constant or slightly elliptical, with the maximum value of SERR in the center of the specimen. For small values of *a/b*, the SERR distribution transitions to bi-modal, with peaks close to the support and loading pins. The rather significant change in SERR distribution with *a/b* correlates well with the C-scan analysis of damage initiation in ECT specimens with $\theta = 90°$, as described in [16] (i.e., delamination front shapes determined from C-scans in [16] are consistent with the strain energy release rate distributions in Fig. 4).

Figure 5 depicts $G_T$ (averaged across specimen width) plotted as a function of *a/b*. The filled circular symbols correspond to $G_T$ calculated from the FE models using VCCT and are used as baseline values against which the other values are compared. The continuous and dashed lines correspond to $G_T$ from simulated MSCC, using the four distinct expressions for $G_T$ in Eqs. 1 to 4. The first two curves (dash-dot and dot) correspond to $G_T$ from simulated MSCC using Eqs. 1 and 2, respectively. The remaining two curves (solid and dashed) correspond to $G_T$ from simulated MSCC using Eqs. 3 and 4 respectively.

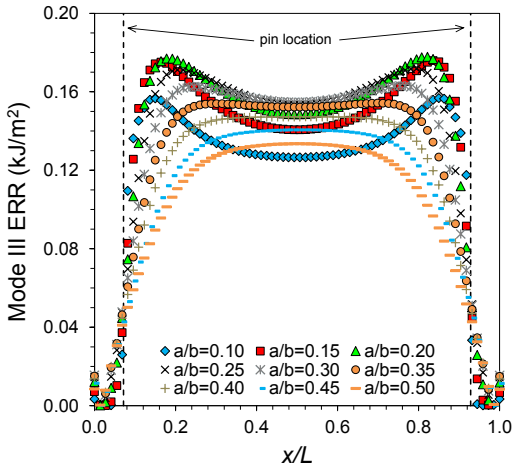


Figure 4. Distribution of computed mode-III energy release rate across delamination front as a function of normalized crack length *a/b* for specimens with $\theta$ of 30°.

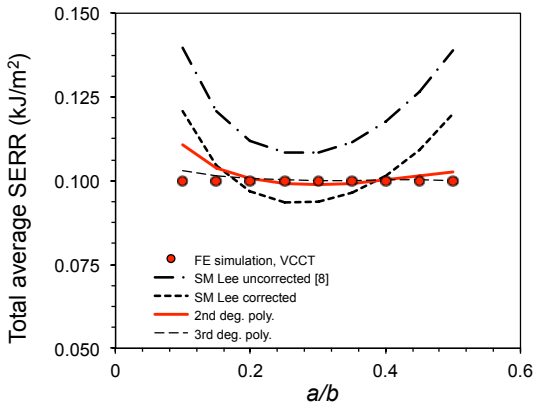


Figure 5. Comparison of total SERR extracted based on VCCT (red circles) and simulated multi-specimen compliance calibration (solid and dashed lines).

In Fig. 5, values of $G_T$ using Eq. 1 do not agree with the VCCT-derived values, suggesting the expression in Eq. 1 does not accurately capture the change of compliance with crack length, *dC/da*. As expected, the corrected version of this expression (Eq. 2) shifts the entire curve downward, without changing its shape. The expressions for $G_T$ from Eqs. 3 and 4 appear to provide a much better correlation with $G_T$ calculated from VCCT; however, both slightly overestimate $G_T$ at the end points (at a/b=0.1 and 0.5). This discrepancy is likely related to errors in polynomial regression arising at end points of the *C* vs. *a* data. Nevertheless, Eq. 4 gives the best correlation between $G_T$ from simulated MSCC and VCCT, thus it is recommended for calculating mode-III fracture toughness, $G_{IIIc}$. Note that this expression for $G_{IIIc}$ assumes that delamination advance occurs uniformly across the entire specimen width, L. Evidence from strain energy release rate distributions (Fig. 4) and C-scans of ECT specimens with grown delaminations (see Fig. 7 in the following discussion) suggests otherwise, indicating that delamination initiation occurs in localized regions along the specimen width. Therefore, the values of $G_{IIIc}$

from Eq. 4 should somehow be corrected to account for the discrepancy between what is assumed in Eq. 4 and what is known to occur in actual ECT specimens. Such a correction is not provided in this study, however.

## Initiation toughness results

The force–displacement data of specimens with $\theta = 0°$, 15°, 30°, and 90° are presented in Figs. 6a-d, respectively. The force-displacement data for specimens with other values of $\theta$ were qualitatively similar and are not shown. Note that individual labels inside of each sub-figure correspond to actual values of *a/b* measured after specimen machining. The figure shows that the load-displacement behavior for all specimens, except those with $\theta = \pm 75°$ (not shown) and $\theta = 90°$, was linear until the peak force was reached.

Time-of-flight C-scan data for representative samples from each of the seven plates tested are shown in Fig. 7. In this figure, the dark gray background in the upper portion of each image corresponds to the back-surface reflection. The bright nearly-white rectangular region on the bottom of each image (e.g., see the upper-left image) corresponds to the PTFE insert starter crack. The curved regions emanating from the PTFE insert correspond to various types of damage resulting from the test. As seen in the figure, specimens with 0° and 90° interface plies exhibited delamination growth that migrated to the ply interface below the midplane. This is evident from the distinct horizontal line separating the PTFE insert and the new damage. As reported previously [16], for specimens with $\theta = 90°$, delamination migration occurred due to coalescence of intralaminar cracks forming in midplane plies. Specimens with $\theta = 45°$, 60°, and 75° exhibited some intralaminar cracking in the midplane plies, but delamination extension remained in the midplane. Finally, specimens with $\theta = 15°$ and 30° exhibited pure delamination extension without any other forms of fracture/damage (i.e., no intralaminar cracking in the midplane plies). The above observations were confirmed by sectioning and optical microscopy of a selected few specimens from each group.

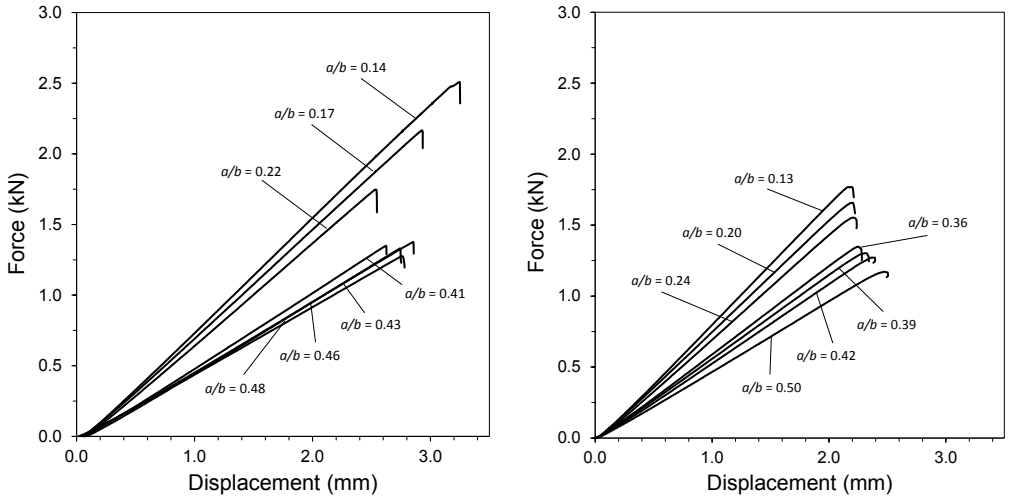


(a) 0°/0° interface (b) +15°/-15° interface

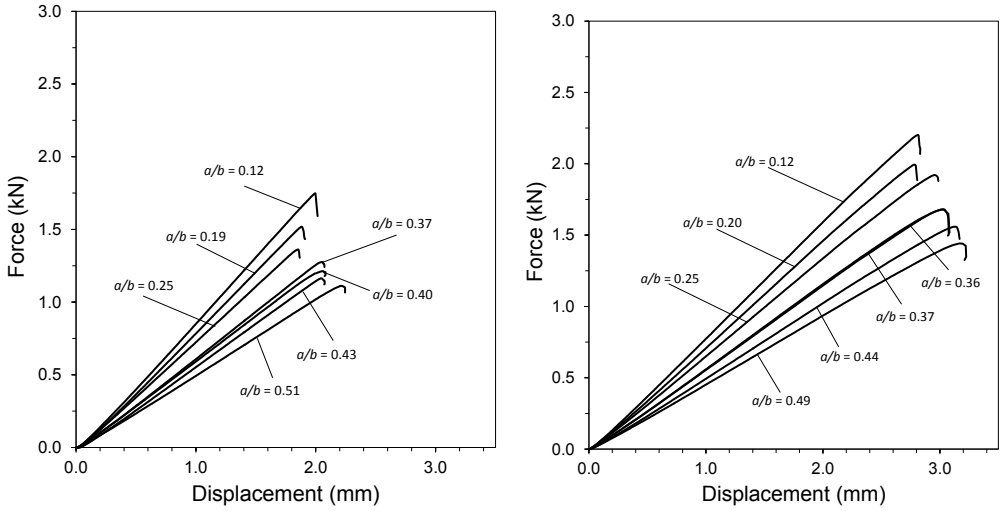


(c) +30°/-30° interface (d) 90°/90° interface

Figure 6. Force–displacement data from plates with (a) 0°/0° interface, (b) +15°/-15° interface, (c) +30°/-30° interface, and (d) 90°/90° interface.

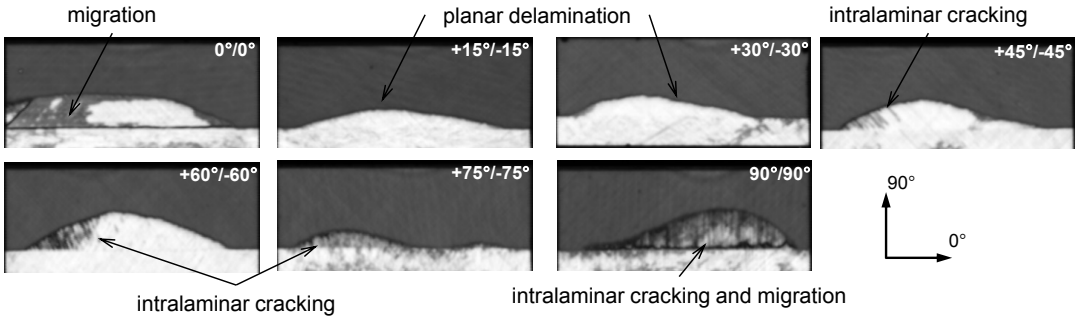


Figure 7. C-scan images of specimens with different ply-orientation angles after the first increment of loading (a/b ≅ 0.23).

Figure 8 presents the experimental and simulated compliance data as a function of crack length, for specimens with $\theta$ = 30°. The experimental compliance data were extracted from the force-displacement curves, based on linear regression over a load range of 0.4 to 0.9 kN. As seen in the figure, there is very good agreement between both data sets, reinforcing the conclusions from the FE simulations discussed previously.

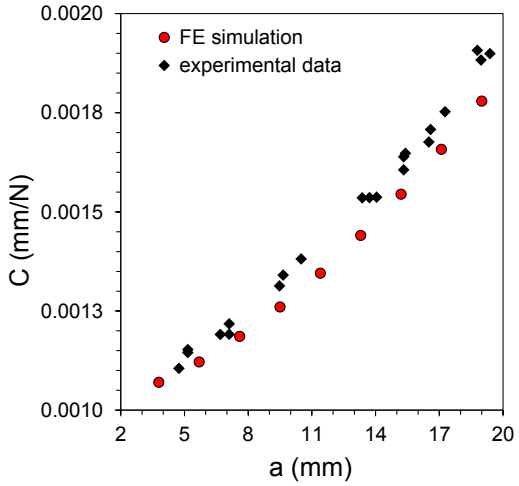


Figure 8. Experimental and computed compliance of the ECT specimen with $\theta$ = 30°, as a function of initial delamination length, *a*.

All of the 21 experimental data points shown in Fig. 8 were fitted with a 3rd-degree polynomial, and the resulting constant coefficients (p1, p2, and p3) were used in Eq. 4 to compute $G_{IIIc\text{-}ave}$ for each specimen. Note that the experimental data in Fig. 8 can be fitted equally well with the compliance solution described in [8]; however, as discussed previously, this expression yields an incorrect form of *dC/da*. Equation 4 was used to calculate $G_{IIIc\text{-}ave}$ for all specimens in the second column of Table II. The summary of these calculations is presented in Fig. 9 as a function of $\theta$, where each solid symbol ($\theta$ = 15° and 30°) corresponds to $G_{IIIc\text{-}ave}$ averaged across the range of *a/b* considered. The open circles in Fig. 9 correspond to specimen geometries for which intralaminar cracking and/or delamination migration were observed. In the figure, the error bars correspond to minimum and

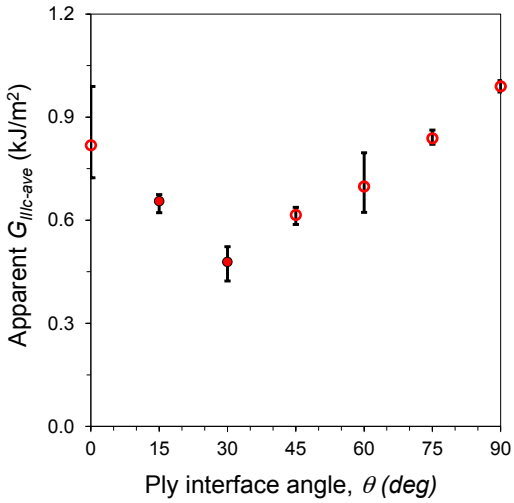


Figure 9. The apparent mode-III fracture toughness as a function of midplane-ply interface angle $\theta$.

maximum values of $G_{IIIc\text{-}ave}$ measured for each $\theta$. Note that in this, and all subsequent plots, $G_{IIIc\text{-}ave}$ is referred to as "apparent" for the following reasons: (1) It is currently unclear how to correct $G_{IIIc\text{-}ave}$ calculated using Eq. 4 to account for localized delamination growth that is known to occur; and (2) as shown in Fig. 7, for certain values of $\theta$, $G_{IIIc\text{-}ave}$ incorporates the energy associated with delamination migration and intralaminar cracking.

An examination of Fig. 9 shows that specimens with $\theta = 30°$ have the lowest apparent $G_{IIIc\text{-}ave}$ at 0.5 kJ/m$^2$, which may be because planar delamination growth is the only energy dissipative mechanism in these specimens. Interestingly, specimens with $\theta = 15°$ also exhibited planar delamination growth in the midplane, and yet the apparent $G_{IIIc\text{-}ave}$ is higher at 0.66 kJ/m$^2$. No obvious explanation for this discrepancy could be found, though it may be possible that undetected energy dissipating mechanisms other than midplane delamination occurred in specimens with $\theta = 15°$. Increasing the midplane ply angle from $\theta = 30°$ to 90° at 15° intervals increases $G_{IIIc\text{-}ave}$ almost linearly. This increase can be related to an increase in frequency of intralaminar cracks in the midplane plies, as summarized in Fig. 10. The crack linear density shown in Fig. 10 was obtained by dividing the number of cracks within the midplane plies by the specimen width, L. Considered together, Figs. 9 and 10 show a clear correlation between the increasing apparent $G_{IIIc\text{-}ave}$ and increasing linear density of cracks (at least for $\theta \geq 30°$). Specifically, the increase in apparent $G_{IIIc\text{-}ave}$ is likely caused by an increased effective crack surface area, which is not accounted for in Eq. 4.

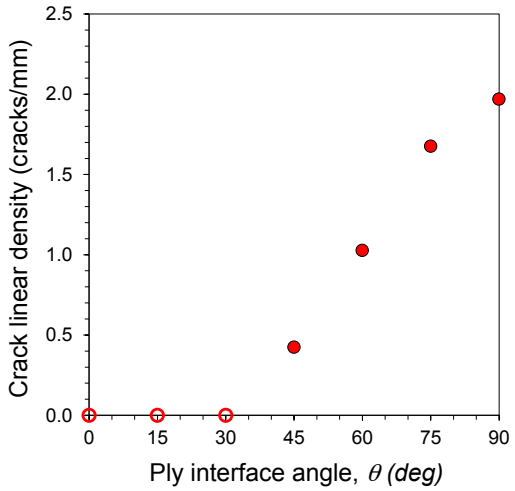


Figure 10. The linear density of intralaminar cracks in the midplane plies as a function of midplane-ply interface angle $\theta$. The open symbols correspond to interfaces where no intralaminar cracks were observed. For $\theta = 0°$, crack migration was observed prior to formation of intralaminar cracks.

## CONCLUSIONS

Several examinations of the edge crack torsion test have revealed two main uncertainties associated with the use of this test method for measuring $G_{IIIc}$ of a composite FRP tape laminate material. First, the data reduction method originally proposed to compute $G_{IIIc}$ from the test data yields values of $G_{III}$ that are inconsistent with values calculated using local methods (i.e., VCCT). A number of possible modifications to the data reduction method have thus been proposed to circumvent this issue. A G-solution that uses a 3$^{rd}$-order polynomial expression for specimen compliance was found to yield values of $G_{III}$ that agree with VCCT-based values. However, further work is required: (1) to provide a correction to the fracture toughness calculation to account for local delamination growth initiation; and (2) to determine a version of this correction method that would be suitable for use in a standardized testing method. Test results of the original ECT specimen showed that plies neighboring the preimplanted insert were unable to contain intralaminar cracks, due to the orientation of these plies. Tests of specimens with these midplane plies positioned at other orientations showed that the intralaminar cracking was contained for midplane ply angles of 15° and 30°. However, values of $G_{IIIc}$ measured using specimens with these two ply orientations were not consistent. Overall, the findings from this study show that there may be promise in the use of ECT for measuring $G_{IIIc}$, however, the issues discussed above must be resolved before the test can be deemed to be reliable.

## REFERENCES


1. O'Brien, T.K. 1982. "Characterization of Delamination Onset and Growth in a Composite Laminate," *Damage in Composite Materials: Basic Mechanisms, Accumulation, Tolerance, and Characterization*, ASTM STP 775, ASTM International: 140-167.
2. ASTM International. Standard Test Method for Mode I Interlaminar Fracture Toughness of Unidirectional Fiber-Reinforced Polymer Matrix Composites, ASTM Standard D5528-13; 2013.
3. ASTM International. Standard Test Method for Mode II Interlaminar Fracture Toughness of Unidirectional Fiber-Reinforced Polymer Matrix Composites, ASTM Standard D7905-14; 2014.
4. ASTM International. Standard Test Method for Mixed Mode I-Mode II Interlaminar Fracture Toughness of Unidirectional Fiber Reinforced Polymer Matrix Composites, ASTM Standard D6671-06; 2013.
5. Donaldson, S.L. 1998. "Mode III Interlaminar Fracture Characterization of Composite Materials," *Compos. Sci. Technol.*, 32(3):225–49.
6. Robinson, P., and D.Q. Song. 1992. "A New Mode III Delamination Test for Composites," *Adv. Compos. Lett*., 1:160-164.
7. Sharif, F., M.T. Kortschot, and R.H. Martin. 1995. "Mode III Delamination Using a Split Cantilever Beam," in *Composite Materials: Fatigue and Fracture*, Martin RH, ed. ASTM STP 1230, ASTM International: 85-99.
8. Lee, S.M. 1993. "An Edge Crack Torsion Method for Mode III Delamination Fracture Testing," *J. Compos. Technol. Res*., 15(3):193-201.
9. Li, J., and T. K. O'Brien. 1996. "Simplified Data Reduction Methods for the ECT Test for Mode III Interlaminar Fracture Toughness," *J. Compos. Technol. Res*., 18(1): 96-101.
10. Ratcliffe, J.G. 2004. "Characterization of the Edge Crack Torsion (ECT) Test for Mode III Fracture Toughness Measurement of Laminated Composites," NASA-TM-2004-213269.
11. de Morais, A.B., A.B. Pereira, M.F.S.F. de Moura, and A.G. Magalhães. 2009. "Mode III Interlaminar Fracture of Carbon/Epoxy Laminates using the Edge Crack Torsion (ECT) Test," *Compos. Sci. Technol*., 69(5):670-676.
12. Li X., L.A. Carlsson, and P. Davies. 2004. "Influence of Fiber Volume Fraction on Mode III Interlaminar Fracture Toughness of Glass/Epoxy Composites," *Comp. Sci. Technol*., 65(2):295-300.
13. de Morais, A.B., AB. Pereira, and M.F.S.F. de Moura. 2011. "Mode III Interlaminar Fracture of Carbon/Epoxy Laminates using the Six-Point Edge Crack Torsion (6ECT)," *Compos. Part A*., 42(11):1793-1799.
14. Pennas, D., W.J. Cantwell, and P. Compston. 2007. "The Influence of Strain Rate on the Mode III Interlaminar Fracture of Composite Materials," *J. Compos. Mater*., 41(21): 2595–2614.
15. Browning, G., L.A. Carlsson, and J.G. Ratcliffe. 2011. "Modification of the Edge Crack Torsion Specimen for Mode III Delamination Testing. Part II – Experimental Study," *J. Compos. Mater*., 45(25): 2633-2640.
16. Czabaj, M.W., J.G. Ratcliffe, and B.D. Davidson. 2013. "Observation of Intralaminar Cracking in the Edge Crack Torsion Specimen," *Eng. Frac. Mech*., 120: 1-14.
17. Greenhalgh, E.S., C. Rogers, and P. Robinson. 2009. "Fractographic Observations on Delamination Growth and the Subsequent Migration Through the Laminate," *Compo. Sci. Tech*., 69(14): 2345-2351.
18. Johnston, A.L., B.D. Davidson, and K.K. Simon. 2014. "Assessment of Split-Beam-Type Tests for Mode III Delamination Toughness Determination," *Int. J. Fract*., 185(1-2):31-48.
19. http://hexcel.com, 2007.
20. Rybicki, E.F. and M.F. Kanninen. 1977. "A Finite Element Calculation of Stress Intensity Factors by a Modified Crack-closure Integral," *Eng. Frac. Mech*., 9:931-938.
21. Krueger, R. 2004. "Virtual Crack Closure Technique: History, Approach, and Applications," *App. Mech. Rev*., 57(2): 109-143.